Wetting transition: Macroscopic roughness, static friction, and energy barrier

Lisen Bi
Institute for Applied Materials—Microstructure Modelling and Simulation (IAM-MMS), Karlsruhe Institute of Technology (KIT), Strasse am Forum 7, 76131 Karlsruhe, Germany

Fei Wang*
Institute for Applied Materials—Microstructure Modelling and Simulation (IAM-MMS), Karlsruhe Institute of Technology (KIT), Strasse am Forum 7, 76131 Karlsruhe, Germany and Institute of Nanotechnology (INT), Karlsruhe Institute of Technology (KIT), Hermann-von-Helmholtz-Platz 1, 76344 Eggenstein-Leopoldshafen, Germany

Britta Nestler
Institute for Applied Materials—Microstructure Modelling and Simulation (IAM-MMS), Karlsruhe Institute of Technology (KIT), Strasse am Forum 7, 76131 Karlsruhe, Germany; Institute of Nanotechnology (INT), Karlsruhe Institute of Technology (KIT), Hermann-von-Helmholtz-Platz 1, 76344 Eggenstein-Leopoldshafen, Germany; and Institute of Digital Materials Science, Karlsruhe University of Applied Sciences, Moltkestrasse 30, 76133 Karlsruhe, Germany

(Received 7 March 2025; accepted 25 September 2025; published 23 October 2025)

When a droplet is deposited on a rough solid substrate, the classic Cassie-Wenzel theory (CWT) is often used to describe the wetting states. However, CWT fails to explain experimental observations of high static friction on hydrophobic surfaces with a critical roll-off angle close to 90°; the static friction is associated with the minimum energy required for the transition between the Cassie state and the Wenzel state. Here, we propose an alternative theory for calculating the static friction force of a droplet on a rough solid surface, based on a complete energy landscape method. Our results for static friction are orders of magnitude larger than those predicted by CWT and have been validated through quantitative comparisons with experiments.

DOI: 10.1103/ybmh-5k99

I. INTRODUCTION

Wetting phenomena [1] play a fundamental role in both natural processes, e.g., the self-cleaning effect on lotus leaves [2], and technological applications, such as coating [3]. The classical Young's theory [4], known as Young's law, is applied for the wetting phenomena of a droplet on a smooth and homogeneous solid substrate. However, most realistic surfaces are rough, causing significant deviations from Young's law. The Cassie-Wenzel theory (CWT) [5,6] extends Young's law via considering the actual contact area between the solid and fluids, caused by the macroscopic surface roughness. CWT identifies two distinct wetting states: the Cassie state, where the droplet sits on top of air pockets trapped within surface asperities [Fig. 1(a)(i)], and the Wenzel state, where the liquid fully wets the rough substrate [Fig. 1(a)(iii)]. CWT is essential for predicting the apparent contact angle on rough surfaces and has significantly advanced the design of surfaces with tailored wetting properties [7–14]. However, it is limited to two idealized states [15–17], neglecting intermediate wetting states [Fig. 1(a)(ii)] as well as the continuous transition between all possible metastable states.

Critically, CWT fails to explain a key experimental observation [18]: the high static friction of a droplet on rough hydrophobic surfaces, where the critical roll-off angle surprisingly approaches 90°—a phenomenon that defies conventional expectations. The failure of CWT arises from the unclear relationship between the static friction [19,20] and the energy barrier [21–23] for the Cassie-Wenzel transition. Experimentally characterizing this transition [24–26] is highly challenging due to the difficulty of tracking the liquid-air interface within submicrometer-scale pores of the surface asperities. While atomistic studies [27–29] have provided valuable insight into the Cassie-Wenzel transition at the nanoscale, they cannot address the multiscale nature of the system, where droplet size and surface roughness span orders of magnitude.

In this work, we address this fundamental gap by introducing a key parameter ξ, which represents the effective solid-liquid contact fraction during the Cassie-Wenzel transition. This approach allows us to construct a comprehensive energy landscape that spans the Cassie, Wenzel, and many other intermediate wetting states. For the first time, we quantify the energy barrier of the Cassie-Wenzel transition, revealing its intricate dependence on the surface roughness.

*Contact author: fei.wang@kit.edu

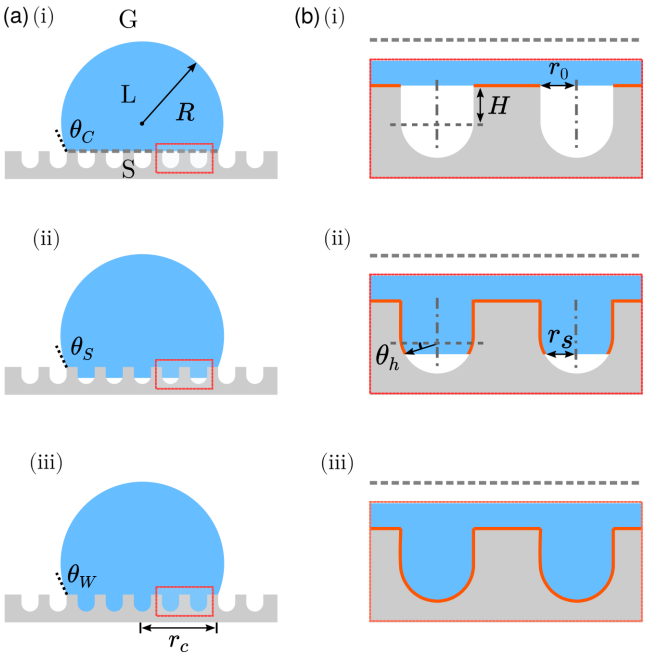

FIG. 1. (a) Schematic sectional view for different wetting states of a sessile droplet on a rough solid surface: (i) Cassie state, (ii) intermediate state, and (iii) Wenzel state. G: gas; L: liquid; and S: solid. (b) A magnified view of the red box in panel (a), highlighting the evolution of ξ—the fraction of liquid-solid contact area (solid red line) relative to the projected area of the droplet's base (dashed gray line)—as the liquid progressively infiltrates or withdraws from the pores.

Crucially, we demonstrate that the static friction of droplets on rough surfaces is intrinsically linked to the saddle point in our energy landscape, corresponding to an intermediate wetting state that was often overlooked previously. This insight forms the basis for an alternative model that accurately predicts static friction forces and explains the high roll-off angles observed in experiments, as validated by quantitative comparisons with various experimental results.

II. THEORETICAL MODEL

We consider a droplet with a given volume $V = 4\pi R_0^3/3$ (where R_0 is an imaginary sphere radius), forming an apparent contact angle θ on a rough solid substrate. For the present consideration of Bond number much less than unity, we express the total energy [30,31] of the system as

$$E = \sum_{i=0}^{N} \int_{A_i} \sigma \, dA_i + \int_S (\gamma_L - \gamma_G) dS, \tag{1}$$

where σ, γ_L, and γ_G are the interfacial energies of liquid-gas, liquid-solid, and gas-solid interfaces, respectively; A_0 depicts the surface area of the capped droplet-gas interface, $A_i (i = 1, 2, \ldots, N)$ is the surface area of the ith liquid-gas interface within the pore beneath the droplet, and S represents the actual contact area between the liquid and the solid substrate.

We consider that the rough solid substrate features pores with an average radius r_0, each composed of a cylindrical upper section and a hemispherical lower section [Fig. 1(b)]. The pore size characterized by r_0 is much smaller than the droplet cap radius R, leading to a multiscale physical scenario. Under this assumption, it is reasonable to consider the volume of the droplet outside the pores as constant. Furthermore, based on the Young-Laplace theory, we adopt the necessary equilibrium condition [16,32] that the mean curvature of the liquid-gas interface within the pore is the same as the one of the capped droplet-gas interface. To scrutinize the continuous wetting transition process of a droplet gradually invading or receding from the pores, we introduce an effective solid-liquid contact area ratio ξ as

$$\xi = \frac{S}{B} = \frac{S}{\pi (R \sin\theta)^2}. \tag{2}$$

This parameter represents the ratio of the true solid-liquid contact area (S), which increases as the liquid fills the pores, to the projected area of the droplet's base (B). The base area B is given by $B = \pi r_c^2 = \pi (R \sin\theta)^2$, where r_c depicts the base radius (Fig. 1). A higher value of ξ corresponds to deeper penetration, as illustrated in Fig. 1(b). The minimum and maximum values of ξ, corresponding to the Cassie and the Wenzel states, respectively, have closed-form expressions in our scenario, $\xi_{\min} = 1 - \rho_s \pi r_0^2$ and $\xi_{\max} = 1 + \rho_s \pi r_0^2 + 2\rho_s \pi r_0 H$. Here, ρ_s is the average pore density per unit area of the substrate, with units of mm^{-2}, and H describes the height of the cylindrical part of the pore [see Fig. 1(b)(i)]. The substrate is smooth when $\rho_s = 0$, whereas positive values of ρ_s generate macroscopic surface roughness.

By defining $\Delta\gamma = \gamma_G - \gamma_L$ and substituting the well-known Young's law $\Delta\gamma = \sigma \cos\theta_0$ (θ_0: Young's contact angle) into the energy function of Eq. (1) subject to the volume constraint $V = (\pi/3) R^3 (2 + \cos\theta)(1 - \cos\theta)^2$, the total interfacial energy of the system can be written as (see Appendix A)

$$\frac{E}{\sigma \left(3V\sqrt{\pi}\right)^{2/3}} = \frac{2 - (1 + \cos\theta)\left(\xi \cos\theta_0 - \rho_s \pi r_s^2\right)}{(1 - \cos\theta)^{1/3} (2 + \cos\theta)^{2/3}}. \tag{3}$$

Here, r_s denotes the radius of the circular liquid-gas interface within the pores [Fig. 1(b)(ii)]. When the interface is located in the cylindrical section, we have $r_s = r_0$; when interface is located in the hemispherical section, we have $r_s = r_0 \cos\theta_h$. The angle θ_h depicts the angle between the horizontal radius of the hemisphere and the line connecting the center of the hemisphere to the triple point at the edge of the interface.

By varying θ and ξ in the full energy function domain $\Lambda = \{(\theta, \xi) \mid 0^\circ < \theta < 180^\circ, \ \xi_{\min} \leqslant \xi \leqslant \xi_{\max}\}$, we obtain a complete energy landscape $E^*(\theta, \xi)$ ($E^* = E/\sigma(3V\sqrt{\pi})^{2/3}$) capturing all possible states during the Cassie-Wenzel transition, as depicted in Fig. 2. The energy landscape is constructed from a thermodynamically quasistatic perspective, providing a consistent description of all states. The equilibrium state is determined via applying the principle of energy minimization to the energy landscape $E^*(\theta, \xi)$:

$$\{\min E^*(\theta, \xi) \mid 0^\circ < \theta < 180^\circ, \ \xi_{\min} \leqslant \xi \leqslant \xi_{\max}\}. \tag{4}$$

Noteworthily, unlike classical CWT, which adopts only two discrete values of ξ (Appendix B), our approach treats ξ as an additional degree of freedom. By minimizing the energy E^* with respect to both ξ and θ, we reveal the existence of

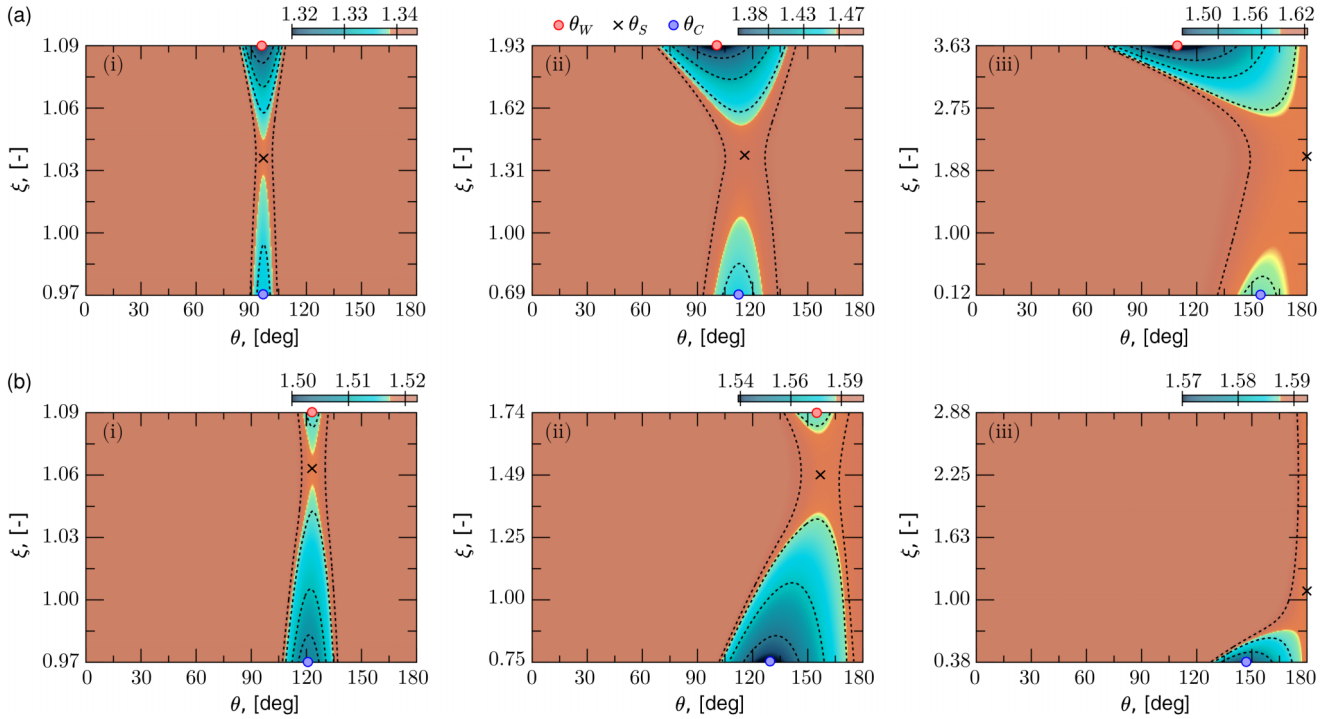

FIG. 2. Energy landscape $E^*(\theta, \xi)$ for solid surfaces with different roughness described by the average pore density per unit area of the substrate ρ_s. (a) The global minimum occurs at $\xi_{\max}$, indicating the Wenzel state with an equilibrium contact angle θ_W (red dot); local minimum at $\xi_{\min}$ representing the Cassie state with an equilibrium contact angle θ_C (blue dot). The cross symbol denotes the saddle point with a contact angle θ_S. The roughness parameters are (i) $\rho_s = 1 \times 10^4\,\mathrm{mm}^{-2}$, (ii) $1 \times 10^5\,\mathrm{mm}^{-2}$, and (iii) $2.8 \times 10^5\,\mathrm{mm}^{-2}$. (b) With increasing ρ_s, we observe a gradual disappearance of the Wenzel state, corresponding to the local minimum at $\xi_{\max}$. The roughness parameters are (i) $1 \times 10^4\,\mathrm{mm}^{-2}$, (ii) $8 \times 10^4\,\mathrm{mm}^{-2}$, and (iii) $2 \times 10^5\,\mathrm{mm}^{-2}$. The Young's contact angles θ_0 in panels (a) and (b) are 95° and 120°, respectively. The energy landscapes illustrate the progressive deviation of θ_C, θ_W, and θ_S from θ_0 as ρ_s increases.

intermediate states and saddle points in the energy landscapes, as highlighted by the cross symbol in Fig. 2. We believe that this strategy is critical for understanding the transition pathway.

III. RESULTS AND DISCUSSION

According to the location of the global minimum in the energy landscapes, we classify the wetting phenomena on rough hydrophobic surfaces into two distinct types, (a) and (b).

Type (a): The global minimum occurs at $\xi_{\max}$ [see Fig. 2(a)]. This type reveals two local energy minima in the energy landscapes, with ξ reaching the maximum and minimum, respectively. These two distinct local energy extrema indicate that the droplet has two equilibrium states: $\xi_{\max}$ corresponds to the Wenzel state with an equilibrium contact angle θ_W, while $\xi_{\min}$ corresponds to the Cassie state with an equilibrium contact angle θ_C. The energy of the system is lower at $\xi_{\max}$, $E^*(\theta_W, \xi_{\max}) < E^*(\theta_C, \xi_{\min})$, indicating that the Wenzel state is more energetically favored. This case has been widely validated in experiments [33–35], where the Cassie state is often regarded as a metastable state [36,37]. Figure 2(a) shows an exemplary energy landscape for type (a) wetting phenomenon with $\theta_0 = 95°$.

Type (b): The global minimum occurs at $\xi_{\min}$ [see Fig. 2(b)]. In this case, the Cassie state, corresponding to $\xi_{\min}$, is the configuration with the lowest energy. In contrast to type (a), which consistently maintains two local energy minima for all surface roughness levels, type (b) exhibits a significant change with increasing ρ_s. The energy landscape in type (b) has a single minimum located at $\xi_{\min}$, as illustrated in Fig. 2(b) (iii) for $\theta_0 = 120°$. This indicates that, at sufficiently high roughness levels, the Cassie state becomes the only stable configuration. Quéré's theory [7] suggests that the Wenzel state is not physical on highly hydrophobic or extremely rough substrates. Here, type (b) supports this idea from an energy perspective.

The complete energy landscape $E^*(\theta, \xi)$ of the Cassie-Wenzel transition and its characteristics under different surface roughness levels (Fig. 2) have the following implications.

A. Wettability

To explore the effect of surface roughness on the apparent contact angle, we derive the equilibrium contact angle as a function of ρ_s, by solving the equation system consisting of $\partial E^*/\partial\theta = 0$ and $\partial E^*/\partial\xi = 0$. The resulting apparent contact angles are expressed in the following closed form as

$$\cos\theta_C = \left(1 - \rho_s \pi r_0^2\right)\cos\theta_0 - \rho_s \pi r_0^2, \tag{5}$$

$$\cos\theta_W = \left(1 + \rho_s \pi r_0^2 + 2\rho_s \pi r_0 H\right)\cos\theta_0. \tag{6}$$

The condition $\cos\theta_C = \cos\theta_W$ corresponds to the point at which the free energies of the Cassie and Wenzel states are

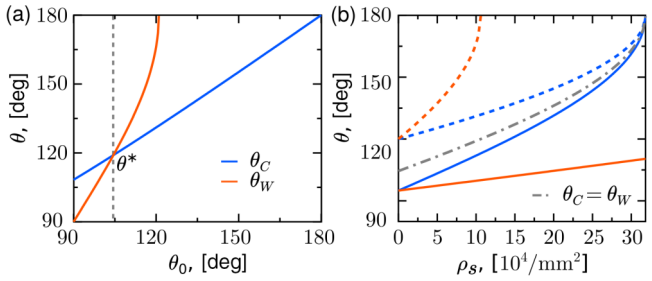

FIG. 3. (a) θ_C [Eq. (5)] and θ_W [Eq. (6)] vs θ_0 for $\rho_s = 1 \times 10^5$ mm^{-2}, with their intersection at θ^* that separates type (a) and type (b) regimes. (b) θ_C (blue line) and θ_W (red line) vs ρ_s for $\theta_0 = 95^\circ$ (solid line), $\theta^* = 104.5^\circ$ (dash-dot line), and $\theta_0 = 120^\circ$ (dashed line); $\theta_C = \theta_W$ at θ^*. In all cases, the structural design parameter is $H/r_0 = 1$.

equal (see Appendix C), marking the transition threshold between the two wetting types. By equating Eq. (5) to Eq. (6), we quantify the threshold θ^* as a function of the structural design parameter H/r_0 as

$$\cos\theta^* = -\frac{1}{2}\left(\frac{1}{1+H/r_0}\right). \tag{7}$$

Figure 3(a) plots θ_C and θ_W as a function of the Young's contact angle θ_0, demonstrating θ^* at their intersection. Parameters are $H/r_0 = 1$ and $\rho_s = 1 \times 10^5$ mm^{-2}.

The variation of the equilibrium contact angle with ρ_s is shown in Fig. 3(b), where $H/r_0 = 1$. We choose $\theta_0 = 95^\circ$ and $\theta_0 = 120^\circ$ as representatives of the two types, (a) and (b), corresponding to Figs. 2(a) and 2(b), respectively. From Fig. 3(b), we see a general trend that both θ_C and θ_W increase with ρ_s. For type (a) (solid lines), θ_W remains smaller than θ_C for any finite roughness ($\rho_s > 0$), consistent with classical wetting theory [38–40], where the Wenzel state enhances wettability. For type (b) (dashed lines), θ_W exceeds θ_C, suggesting an unconventional regime where the Cassie state is energetically favorable despite greater intrinsic wettability. Direct experimental comparison between these states remains challenging, since determining whether a droplet is in the Cassie or Wenzel state requires resolving the liquid-gas interface across multiple scales, which current imaging techniques cannot readily achieve. However, the unconventional regime ($\theta_C < \theta_W$) can emerge during different nucleation stages: (S1) Initial nucleation—For nanoscale droplets comparable to pore size, condensation within surface roughness can initially trap droplets in a Wenzel-like state, even when the Cassie state is energetically favorable [41–45]. (S2) Growth stage—As condensation continues and droplets grow beyond pore dimensions, the system stabilizes in the Cassie state. Although $\theta_C < \theta_W$ and $E_C^* < E_W^*$, the Wenzel state (θ_W) dominates during initial nucleation (S1), while the Cassie state (θ_C) becomes prevalent in the growth stage (S2).

B. Energy barrier

Through the energy landscapes shown in Fig. 2, we clarify another key concept: the minimum energy barrier for the Cassie-Wenzel transition is not the energy difference between the two local minima, but rather the difference between each

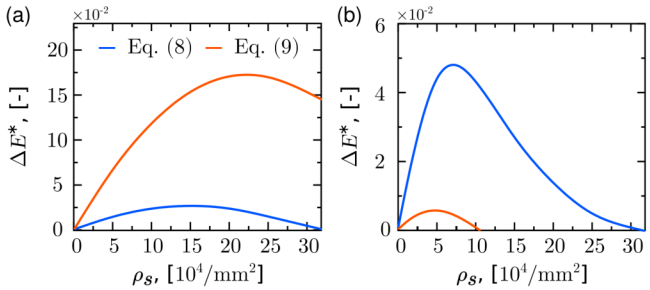

FIG. 4. The energy barrier for the Cassie-to-Wenzel transition ΔE_C^* [Eq. (8)] and the Wenzel-to-Cassie transition ΔE_W^* [Eq. (9)] vs ρ_s for (a) $\theta_0 = 95^\circ$ and (b) $\theta_0 = 120^\circ$, with $H/r_0 = 1$.

minimum and the intermediate saddle point. As such, we propose the energy barrier for the Cassie-Wenzel transition as

$$\Delta E_C^* = E^*(\theta_S, \xi_S) - E^*(\theta_C, \xi_{\min}), \tag{8}$$

$$\Delta E_W^* = E^*(\theta_S, \xi_S) - E^*(\theta_W, \xi_{\max}), \tag{9}$$

where ΔE_C^* and ΔE_W^* represent the energy barriers for Cassie-to-Wenzel and Wenzel-to-Cassie transitions, respectively. $E^*(\theta_S, \xi_S)$, $E^*(\theta_C, \xi_{\min})$, and $E^*(\theta_W, \xi_{\max})$ depict the system energy at the intermediate (saddle point), Cassie, and Wenzel states, respectively. These energy barriers represent the minimum energetic cost required to overcome metastability and trigger a wetting transition, thereby quantifying the stability of each state.

The saddle point emerges naturally along the continuous wetting transition pathway, with its energy landscape governed by surface roughness. This leads to energy barriers that exhibit strong roughness dependence, as shown in Fig. 4. For type (a) wetting [Fig. 4(a)], the Wenzel-to-Cassie transition barrier exceeds the Cassie-to-Wenzel barrier. Conversely, this relationship reverses for type (b) wetting [Fig. 4(b)]. Notably, the energy barriers display nonmonotonic behavior with increasing ρ_s, first rising then decreasing, revealing a more complex dependence than previously assumed.

C. Static friction

Existing frameworks [46–52] for droplet static friction on rough interfaces are predominantly based on the difference between the cosine of the advancing contact angle, $\cos\theta_A$, and the cosine of receding contact angle, $\cos\theta_R$ [53]. In contrast, we here propose an alternative model to calculate the static friction as (see Appendix D)

$$F_f = \omega\sigma(\cos\theta_i - \cos\theta_S), \quad \theta_i \in \{\theta_C, \theta_W\}. \tag{10}$$

The parameter ω depicts the droplet width. According to the energy landscape $E^*(\theta, \xi)$ and the principle of energy minimization, we obtain the closed form for the apparent contact angle of the saddle point θ_S as

$$\cos\theta_S = \cos\theta_0 - \rho_s \pi r_0^2\left[\cos\theta_0^2 - (2H/r_0 - 1)\cos\theta_0 + 1\right].$$

Under the tilted plate method for measuring static friction, Eq. (10) takes the following explicit form (see Appendix E):

$$\rho g V \sin\alpha = \omega\sigma(\cos\theta_i - \cos\theta_S), \quad \theta_i \in \{\theta_C, \theta_W\}, \tag{11}$$

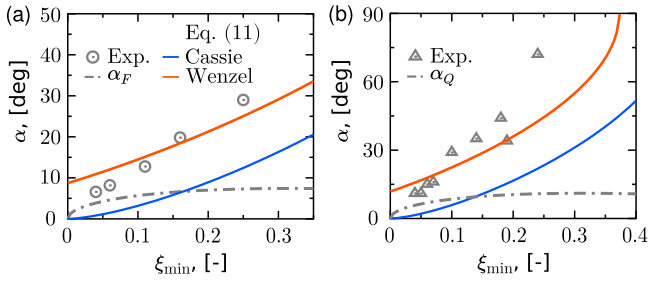

FIG. 5. (a) Comparison of roll-off angle α calculated from Eq. (11) with experiments [46] and Furmidge model α_F [47]. (b) Comparison of α with experiments [18] and Quéré model: α_Q [18].

where ρ is the density of droplet, g depicts the gravity acceleration, and α represents the roll-off angle. Figures 5(a) and 5(b) present a quantitative comparison of α versus $\xi_{\min}$ (solid fraction of the substrate that is varied in experiments) with various experiments [18,46] and existing theories (Furmidge model: α_F [47]; Quéré model: α_Q [18]). To ensure the reasonableness of the comparison, we set the droplet width ω in Eq. (11) to be consistent with the compared models: $\omega = 2r_c$ for α_F and $\omega = \pi r_c$ for α_Q. In our calculations, the value of θ_0 is set in accordance with the experimental conditions: $\theta_0 = 105^\circ$ in Fig. 5(a) and $\theta_0 = 100^\circ$ in Fig. 5(b). For all comparative results, α in our model increases significantly with $\xi_{\min}$, exhibiting a good agreement with experiments, but deviates considerably from the predictions of existing models.

IV. CONCLUSIONS

In conclusion, we have introduced an original concept—the effective solid-liquid contact fraction (ξ)—to describe the Cassie-Wenzel transition, enabling the construction of a complete energy landscape $E^*(\theta, \xi)$ that encompasses the full spectrum of wetting states. This framework has, for the first time, allowed us to precisely quantify the energy barrier of the Cassie-Wenzel transition and its intricate dependence on surface roughness. Importantly, we establish a fundamental link between the static friction of droplets on rough surfaces and the saddle point in the energy landscape, corresponding to the intermediate wetting state. These insights have led to a predictive model that accurately captures the static friction of droplets on rough hydrophobic surfaces and explains the high roll-off angles observed in experiments—resolving long-standing discrepancies between theory and observation.

ACKNOWLEDGMENTS

L.B. thanks for funding of the China Scholarship Council (CSC). F.W. thanks for funding of VirtMat project "VirtMat P09: Wetting Phenomena" of the Helmholtz association, as part of the program "MSE-materials science and engineering" No. 43.31.01.

DATA AVAILABILITY

No data were created or analyzed in this study.

APPENDIX A: DERIVATION OF THE TOTAL FREE ENERGY UNDER THE VOLUME CONSTRAINT

The volume V of a droplet shaped as a spherical cap, with contact angle θ and radius R, is given by

$$V = (\pi/3)R^3(2+\cos\theta)(1-\cos\theta)^2. \tag{A1}$$

The total interfacial energy of the system reads

$$E = \sigma A_0 - \Delta\gamma\xi\pi(R\sin\theta)^2 + \sigma\pi r_s^2\rho_s\pi(R\sin\theta)^2. \tag{A2}$$

Here, the first term represents the liquid-gas interfacial energy of the spherical cap with area $A_0 = 2\pi R^2(1-\cos\theta)$. The second term depicts the free energy due to the replacement of gas-solid interface by a liquid-solid interface. The third term describes the liquid-gas interfacial energy inside the pores beneath the droplet. According to the volume constraint of Eq. (A1), we have the following expression of R as

$$R = \left[\frac{3V}{\pi(1-\cos\theta)^2(2+\cos\theta)}\right]^{\frac{1}{3}}. \tag{A3}$$

Substituting Eq. (A3) and the Young's equation $\Delta\gamma = \sigma\cos\theta_0$ into the energy function of Eq. (A2), we obtain the final expression of total free energy as shown in Eq. (3).

APPENDIX B: DERIVATION OF THE CASSIE AND WENZEL EQUATIONS ACCORDING TO BORMASHENKO'S THEORY

The following derivation of the Cassie and Wenzel equations is based on the approach developed in Ref. [8] and reproduced here for completeness.

For a sessile droplet of fixed volume V resting on a flat, chemically homogeneous solid substrate, the total free energy of the system can be expressed as

$$E_0 = \sigma A_0 + \Delta\gamma\pi(R\sin\theta)^2, \tag{B1}$$

where the first term accounts for the liquid-gas interfacial energy and the second item captures the interfacial energy change due to liquid spreading over the substrate. With the cap radius expression from Eq. (A3) resulting from volume constraint and the definition $a = \Delta\gamma$, one can eliminate R and express E_0 solely as a function of θ:

$$E_0 = \left[\frac{9\pi V^2}{(1-\cos\theta)(2+\cos\theta)^2}\right]^{\frac{1}{3}}[2\sigma - a(1+\cos\theta)].$$

The straightforward differentiation of E_0 with respect to θ gives

$$\frac{dE_0}{d\theta} = \left[\frac{9\pi V^2}{(1-\cos\theta)^4(2+\cos\theta)^5}\right]^{\frac{1}{3}} 2(a-\sigma\cos\theta)\sin\theta.$$

Next, we solve $dE_0/d\theta = 0$, yielding

$$a = \sigma\cos\theta_0, \quad \text{or equivalently,} \quad \cos\theta_0 = \frac{\Delta\gamma}{\sigma}, \tag{B2}$$

which is the Young's equation, and a trivial solution $\theta_0 = 0^\circ$. For a composite surface composed of two types of regions—a solid region with solid fraction ϕ and gas (air) pockets with fractional area coverage $1-\phi$—the effective interfacial energy difference is $a = \phi\Delta\gamma - (1-\phi)$. Substituting this

expression into Eq. (B2), the Cassie equation for the apparent contact angle θ_C reads

$$\cos\theta_C = \phi\cos\theta_0 - (1-\phi). \tag{B3}$$

Consider now a rough surface characterized by the roughness factor $f > 1$, defined as the ratio of the actual liquid-solid contact area to its horizontal projection [6]. The effective interfacial energy difference is then given by $a = f\Delta\gamma$, which, when applied to the equilibrium condition in Eq. (B2), yields the Wenzel equation for the apparent contact angle θ_W:

$$\cos\theta_W = f\cos\theta_0. \tag{B4}$$

The Cassie and Wenzel equations describe two idealized cases of wetting on structured surfaces by relating the apparent contact angle to the roughness parameters ϕ and f. In our scenario, these parameters can be expressed as

$$\phi = \frac{A_{\text{solid}}}{A_{\text{proj}}} = 1 - \rho_s\pi r_0^2,$$

$$f = \frac{A_{\text{actual}}}{A_{\text{proj}}} = 1 + \rho_s\pi r_0^2 + 2\rho_s\pi r_0 H.$$

Here, A_{solid} is the area of the droplet's base in contact with the solid substrate, A_{actual} is the actual solid-liquid contact area, and A_{proj} is the projected area of the droplet's base. From these definitions, it is clear that the parameters $\xi_{\min}$ and $\xi_{\max}$, introduced in our framework [see Eq. (2)], are conceptually equivalent to the classical roughness parameters ϕ and f.

It is worth noting that the equilibrium conditions obtained from free energy minimization (incorporating the volume constraint) are identical to those derived via the Lagrange multiplier method [54].

APPENDIX C: DERIVATION OF THE EQUIVALENCE BETWEEN $\cos\theta_C = \cos\theta_W$ AND THE FREE ENERGY EQUALITY OF THE CASSIE AND WENZEL STATES

Based on the expressions given in Eqs. (3) and (5), the total interfacial energy of the droplet in the Cassie state can be written as

$$\frac{E_C}{\sigma\left(3V\sqrt{\pi}\right)^{2/3}} = \frac{2-(1+\cos\theta_C)\cos\theta_C}{(1-\cos\theta_C)^{1/3}(2+\cos\theta_C)^{2/3}}. \tag{C1}$$

Similarly, combining the expressions in Eqs. (3) and (6), the total interfacial energy of the droplet in the Wenzel state can be expressed as

$$\frac{E_W}{\sigma\left(3V\sqrt{\pi}\right)^{2/3}} = \frac{2-(1+\cos\theta_W)\cos\theta_W}{(1-\cos\theta_W)^{1/3}(2+\cos\theta_W)^{2/3}}. \tag{C2}$$

Assuming that the energies are equal, i.e., $E_C = E_W$, and dividing both sides by the positive quantity $\sigma(3V\sqrt{\pi})^{2/3}$, we obtain

$$F(\cos\theta_C) = F(\cos\theta_W), \tag{C3}$$

where $F(x) = [2-(1+x)x]/(1-x)^{1/3}(2+x)^{2/3}$. Since the volume V is fixed, $F(x)$ is a continuous and strictly monotonic function defined on the physically meaningful domain $x \in (-1, 1)$, as verified by its derivative $F'(x)$. Thus, Eq. (C3) implies

$$\cos\theta_C = \cos\theta_W, \quad \text{and equivalently,} \quad \theta_C = \theta_W. \tag{C4}$$

This result indicates that the threshold between types (a) and (b) occurs precisely at the point where the apparent contact angles of Cassie and Wenzel states are equal, which reflects the equality of the total interfacial free energies of these two states.

APPENDIX D: DERIVATION OF THE STATIC FRICTION

In the presence of contact-angle hysteresis [Fig. 6(a)], the local static friction per unit length at the advancing (f_A) and receding (f_R) contact lines read [55]

$$f_A = \sigma(\cos\theta_A - \cos\theta_0), \quad f_R = \sigma(\cos\theta_R - \cos\theta_0).$$

Here, θ_A and θ_R are the advancing and receding contact angles, respectively. For the total static friction along the contact line F_f, two interpretations emerge based on the directionality of the local static friction per unit length:

(1) Normal to the local tangent of the contact line [Fig. 6(b)]. The total friction contributions from the advancing and receding parts of the contact line read $F_{A/R} = 2\int_0^{\pi/2} f_{A/R} r_c \cos\eta\, d\eta$, where η depicts the azimuthal angle. Thus, the total static friction F_f becomes

$$F_f = F_R - F_A = 2r_c\sigma(\cos\theta_R - \cos\theta_A). \tag{D1}$$

(2) Parallel to the direction of the droplet's impending motion [Fig. 6(c)]. The total static friction on the advancing and receding sides is written as $F_{A/R} = 2\int_0^{\pi/2} r_c f_{A/R} d\eta$. After integration, we obtain the total static friction as

$$F_f = F_R - F_A = \pi r_c\sigma(\cos\theta_R - \cos\theta_A). \tag{D2}$$

Note that both $2r_c$ and πr_c in the total static friction expressions of Eqs. (D1) and (D2) describe droplet's lateral dimension, leading to the uniform expression of F_f as

$$F_f = \omega\sigma(\cos\theta_R - \cos\theta_A), \tag{D3}$$

where ω represents the characteristic droplet width. The above derivation only accounts for the energy difference between two (meta)stable states—namely, the advancing and receding states, which correspond to the Wenzel and Cassie states in the context of surface roughness [50–52]. However, to capture the actual depinning threshold associated with the energy barrier, we propose a more general expression based on our energy map method:

$$F_f = \omega\sigma(\cos\theta_i - \cos\theta_S), \quad \theta_i \in \{\theta_C, \theta_W\}. \tag{D4}$$

Here, θ_S, θ_C, and θ_W denote the contact angles at the intermediate saddle-point state, Cassie state, and Wenzel state, respectively. The advancing contact angle θ_A is defined as the maximum contact angle that a droplet can sustain before the contact line advances. From this definition, θ_S corresponds to θ_A in our model, as it represents the maximum contact angle along the most probable thermodynamic pathway of the wetting transition.

We emphasize that the above derivation only accounts for the static friction arising from wetting transitions on macroscopic rough surfaces. For cases where static friction and contact-angle hysteresis occur even on macroscopically smooth surfaces, we refer readers to a recent

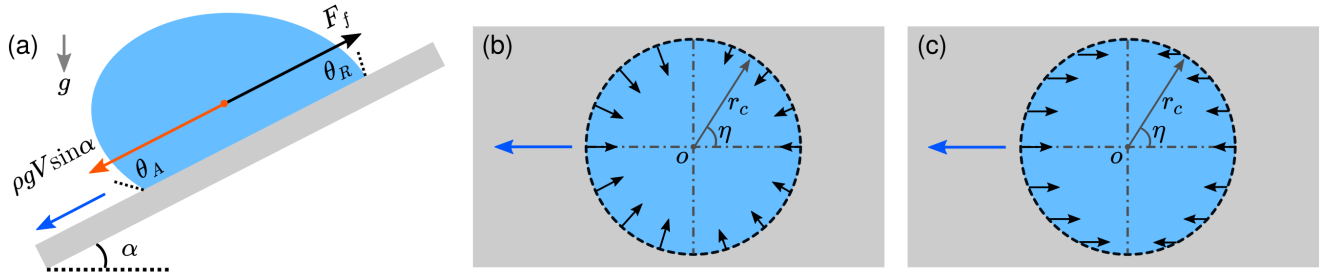

FIG. 6. (a) Sectional view of a droplet with volume V at the critical sliding state with the roll-off angle α, the advancing and receding contact angles (θ_A and θ_R), the tangential component of the gravity $\rho gV \sin\alpha$ (orange arrow), and the static friction (black arrow). (b) and (c) Bottom views of a droplet at the critical sliding state using the tilted plate method, highlighting two interpretations of the local static friction's direction (black arrow). In panel (b), the static friction is normal to the local tangent of the contact line, while in panel (c), it is parallel to the direction of impending motion (blue arrow).

work [31], which explicitly addresses how microscopic surface effects give rise to contact-angle hysteresis and static friction.

APPENDIX E: DERIVATION OF THE ROLL-OFF ANGLE

A standard technique for measuring static friction is the tilted plate method. In this approach, a droplet of volume V is deposited on an adjustable plate that is slowly inclined. The droplet remains pinned by static friction until the gravitational force component parallel to the surface exceeds the frictional resistance. The critical inclination angle α at which sliding initiates is defined as the roll-off angle [Fig. 6(a)]. The parallel gravitational component is given by $F_\parallel = \rho gV \sin\alpha$. Sliding commences when this force balances the static friction threshold. Using the static friction formulation in Eq. (10), this equilibrium condition yields the closed-form solution presented in Eq. (11).

[1] P.-G. de Gennes, Wetting: statics and dynamics, Rev. Mod. Phys. **57**, 827 (1985).

[2] K. Koch, B. Bhushan, and W. Barthlott, Multifunctional surface structures of plants: An inspiration for biomimetics, Prog. Mater. Sci. **54**, 137 (2009).

[3] F. Wang, Y. Wu, and B. Nestler, Wetting effect on patterned substrates, Adv. Mater. **35**, 2210745 (2023).

[4] T. Young, III. An essay on the cohesion of fluids, Philos. Trans. R. Soc. London **95**, 65 (1805).

[5] A. Cassie and S. Baxter, Wettability of porous surfaces, Trans. Faraday Soc. **40**, 546 (1944).

[6] R. N. Wenzel, Resistance of solid surfaces to wetting by water, Ind. Eng. Chem. **28**, 988 (1936).

[7] A. Lafuma and D. Quéré, Superhydrophobic states, Nat. Mater. **2**, 457 (2003).

[8] G. Whyman, E. Bormashenko, and T. Stein, The rigorous derivation of young, Cassie–Baxter and Wenzel equations and the analysis of the contact angle hysteresis phenomenon, Chem. Phys. Lett. **450**, 355 (2008).

[9] E. Bormashenko, R. Pogreb, G. Whyman, and M. Erlich, Cassie–Baxter wetting transition in vibrating drops deposited on rough surfaces: Is the dynamic Cassie-Baxter wetting transition a 2D or 1D Affair? Langmuir **23**, 6501 (2007).

[10] J. Sun, P. Zhu, X. Yan, C. Zhang, Y. Jin, X. Chen, and Z. Wang, Robust liquid repellency by stepwise wetting resistance, Appl. Phys. Rev. **8**, 031403 (2021).

[11] J. Wu, R. Ma, Z. Wang, and S. Yao, Do droplets always move following the wettability gradient? Appl. Phys. Lett. **98**, 204104 (2011).

[12] Z. Guo, Y. Liu, D. Lohse, X. Zhang, and X. Zhang, Stability of micro-Cassie states on rough substrates, J. Chem. Phys. **142**, 244704 (2015).

[13] J. M. Encarnación Escobar, D. García-González, I. Dević, X. Zhang, and D. Lohse, Morphology of evaporating sessile microdroplets on lyophilic elliptical patches, Langmuir **35**, 2099 (2019).

[14] S. Peng, T. L. Mega, and X. Zhang, Collective effects in microbubble growth by solvent exchange, Langmuir **32**, 11265 (2016).

[15] I. W. Park, J. M. Ribe, M. Fernandino, and C. A. Dorao, The criterion of the Cassie–Baxter and Wenzel wetting modes and the effect of elastic substrates on it, Adv. Mater. Interfaces **10**, 2202439 (2023).

[16] A. Marmur, Wetting on hydrophobic rough surfaces: To be heterogeneous or not to be? Langmuir **19**, 8343 (2003).

[17] A. Marmur and E. Bittoun, When Wenzel and Cassie are right: Reconciling local and global considerations, Langmuir **25**, 1277 (2009).

[18] M. Reyssat and D. Quéré, Contact angle hysteresis generated by strong dilute defects, J. Phys. Chem. B **113**, 3906 (2009).

[19] N. Gao, F. Geyer, D. W. Pilat, S. Wooh, D. Vollmer, H.-J. Butt, and R. Berger, How drops start sliding over solid surfaces, Nat. Phys. **14**, 191 (2018).

[20] R. Tadmor, Open problems in wetting phenomena: Pinning retention forces, Langmuir **37**, 6357 (2021).

[21] E. Bormashenko, Progress in understanding wetting transitions on rough surfaces, Adv. Colloid Interface Sci. **222**, 92 (2015).

[22] G. Whyman and E. Bormashenko, Wetting transitions on rough substrates: General considerations, J. Adhes. Sci. Technol. **26**, 207 (2012).

[23] C. Ishino, K. Okumura, and D. Quéré, Wetting transitions on rough surfaces, Europhys. Lett. **68**, 419 (2004).

[24] M. Xu, G. Sun, and C.-J. Kim, Infinite lifetime of underwater superhydrophobic states, Phys. Rev. Lett. **113**, 136103 (2014).

[25] P. Lv, Y. Xue, Y. Shi, H. Lin, and H. Duan, Metastable states and wetting transition of submerged superhydrophobic structures, Phys. Rev. Lett. **112**, 196101 (2014).

[26] Y. Xiang, S. Huang, P. Lv, Y. Xue, Q. Su, and H. Duan, Ultimate stable underwater superhydrophobic state, Phys. Rev. Lett. **119**, 134501 (2017).

[27] T. Koishi, K. Yasuoka, S. Fujikawa, T. Ebisuzaki, and X. C. Zeng, Coexistence and transition between Cassie and Wenzel state on pillared hydrophobic surface, Proc. Natl. Acad. Sci. USA **106**, 8435 (2009).

[28] A. Giacomello, M. Chinappi, S. Meloni, and C. M. Casciola, Metastable wetting on superhydrophobic surfaces: Continuum and atomistic views of the Cassie-Baxter–Wenzel transition, Phys. Rev. Lett. **109**, 226102 (2012).

[29] T.-H. Yen and C.-Y. Soong, Hybrid Cassie–Wenzel model for droplets on surfaces with nanoscale roughness, Phys. Rev. E **93**, 022805 (2016).

[30] F. Wang, H. Zhang, and B. Nestler, Wetting phenomena: Line tension and gravitational effect, Phys. Rev. Lett. **133**, 246201 (2024).

[31] F. Wang and B. Nestler, Wetting and contact-angle hysteresis: Density asymmetry and van der Waals force, Phys. Rev. Lett. **132**, 126202 (2024).

[32] F. Wang, H. Zhang, Y. Wu, and B. Nestler, A thermodynamically consistent diffuse interface model for the wetting phenomenon of miscible and immiscible ternary fluids, J. Fluid Mech. **970**, A17 (2023).

[33] J. Long, L. Pan, P. Fan, D. Gong, D. Jiang, H. Zhang, L. Li, and M. Zhong, Cassie-state stability of metallic superhydrophobic surfaces with various micro/nanostructures produced by a femtosecond laser, Langmuir **32**, 1065 (2016).

[34] O. Bliznyuk, V. Veligura, E. S. Kooij, H. J. Zandvliet, and B. Poelsema, Metastable droplets on shallow-grooved hydrophobic surfaces, Phys. Rev. E **83**, 041607 (2011).

[35] A. Promraksa, Y.-C. Chuang, and L.-J. Chen, Study on the wetting transition of a liquid droplet sitting on a square-array cosine wave-like patterned surface, J. Colloid Interface Sci. **418**, 8 (2014).

[36] G. Whyman and E. Bormashenko, How to make the Cassie wetting state stable? Langmuir **27**, 8171 (2011).

[37] M. Reyssat, J. M. Yeomans, and D. Quéré, Impalement of fakir drops, Europhys. Lett. **81**, 26006 (2007).

[38] B. Bhushan and Y. C. Jung, Natural and biomimetic artificial surfaces for superhydrophobicity, self-cleaning, low adhesion, and drag reduction, Prog. Mater. Sci. **56**, 1 (2011).

[39] D. Quéré, Wetting and roughness, Annu. Rev. Mater. Res. **38**, 71 (2008).

[40] E. Bormashenko, *Wetting of Real Surfaces* (Walter de Gruyter GmbH & Co. KG, Leipzig, 2018), Vol. 19.

[41] B. Zhang, X. Chen, J. Dobnikar, Z. Wang, and X. Zhang, Spontaneous Wenzel to Cassie dewetting transition on structured surfaces, Phys. Rev. Fluids **1**, 073904 (2016).

[42] K. Rykaczewski, A. T. Paxson, S. Anand, X. Chen, Z. Wang, and K. K. Varanasi, Multimode multidrop serial coalescence effects during condensation on hierarchical superhydrophobic surfaces, Langmuir **29**, 881 (2013).

[43] T. Mouterde, G. Lehoucq, S. Xavier, A. Checco, C. T. Black, A. Rahman, T. Midavaine, C. Clanet, and D. Quéré, Antifogging abilities of model nanotextures, Nat. Mater. **16**, 658 (2017).

[44] S. Peng, I. Devic, H. Tan, D. Lohse, and X. Zhang, How a surface nanodroplet sits on the rim of a microcap, Langmuir **32**, 5744 (2016).

[45] D. Lohse and X. Zhang, Surface nanobubbles and nanodroplets, Rev. Mod. Phys. **87**, 981 (2015).

[47] C. Furmidge, Studies at phase interfaces. I. The sliding of liquid drops on solid surfaces and a theory for spray retention, J. Colloid Sci. **17**, 309 (1962).

[48] H. Zhang, H. Zhang, F. Wang, and B. Nestler, Exploration of contact angle hysteresis mechanisms: From microscopic to macroscopic, J. Chem. Phys. **161**, 194705 (2024).

[49] F. Aurbach, F. Wang, and B. Nestler, Wetting phenomena of droplets and gas bubbles: Contact angle hysteresis based on varying liquid–solid and solid–gas interfacial tensions, J. Chem. Phys. **161**, 164708 (2024).

[50] N. A. Patankar, Hysteresis with regard to Cassie and Wenzel states on superhydrophobic surfaces, Langmuir **26**, 7498 (2010).

[51] T. Koishi, K. Yasuoka, S. Fujikawa, and X. C. Zeng, Measurement of contact-angle hysteresis for droplets on nanopillared surface and in the Cassie and Wenzel states: A molecular dynamics simulation study, ACS Nano **5**, 6834 (2011).

[52] H. Y. Erbil, The debate on the dependence of apparent contact angles on drop contact area or three-phase contact line: A review, Surf. Sci. Rep. **69**, 325 (2014).

[53] Existing models [50–52] erroneously equate the contact angles of the Wenzel and Cassie states with the advancing and receding contact angles, respectively, while completely neglecting the critical intermediate state—the saddle point configuration and its corresponding contact-angle characteristics.

[46] C. Lv, C. Yang, P. Hao, F. He, and Q. Zheng, Sliding of water droplets on microstructured hydrophobic surfaces, Langmuir **26**, 8704 (2010).

[54] E. Blokhuis, Y. Shilkrot, and B. Widom, Young's law with gravity, Mol. Phys. **86**, 891 (1995).

[55] J.-F. Joanny and P.-G. De Gennes, A model for contact angle hysteresis, J. Chem. Phys. **81**, 552 (1984).